Reaction Chemistry & Engineering

ROYAL SOCIETY OF CHEMISTRY

PAPER

View Article Online
View Journal | View Issue

Check for updates

Cite this: *React. Chem. Eng.*, 2024, **9**, 2089

Parameter investigation of an organic–inorganic hybrid resin for a 3D-printed microchannel heat exchanger†

Sunjae Lee, ‡ Amirreza Mottafegh‡ and Dong-Pyo Kim *

Received 20th December 2023,
Accepted 18th April 2024

DOI: 10.1039/d3re00694h

rsc.li/reaction-engineering

3D printing photocurable resin facilitates the fabrication of versatile polymer heat exchangers that have advantages of low cost, lightweight, antifouling, and anticorrosion properties over metal heat exchangers but suffer from low thermal stability, mechanical strength, and chemical resistance. Based on the intrinsic intermediate properties of preceramic polymers between polymers and ceramics, an organic–inorganic hybrid resin for a 3D-printed microchannel heat exchanger is formulated by adding an acrylate monomer and optimal cocktails of additives as well as printing parameters. The base resin was prepared by mixing preceramic allylhydridopolycarbosilane (AHPCS) known as a SiC ceramic precursor with 1,6-hexanediol diacrylate (HDDA) to increase the curing kinetics, Sudan Orange G (SOG) as a resolution enhancer, and fumed silica as an anti-sticking agent. The 3D-printed structures from the hybrid resin were thermally post-cured at 260 °C for 3 h to investigate the thermo-physical properties such as modulus, hardness, thermal conductivity, and the coefficient of thermal expansion. Based on the result of computational fluid dynamics (CFD) simulations, the 3D-printed and post-cured tube-in-tube type microchannel heat exchanger (3P-TMHE) was operated under elevated temperature and chemical conditions using DMSO at 70 °C. This study can act as a guideline for printing high-performance heat exchangers using diverse 3D printing technology for resin formulation.

Introduction

Microchannel heat exchangers (MHEs) are a type of heat exchanger that uses microchannels with a hydraulic diameter below 1 mm, to transfer heat between two fluids. The small channel size and volume relatively allow high heat transfer behaviour even with a low amount of refrigerant. The optimal design of the microchannels enables light and compact systems with low flow resistance, which is suitable for applications of air conditioning, refrigeration, heat pumps, and microprocessor cooling.[1–4] Metal-based microchannel heat exchangers, owing to their weight and susceptibility to corrosion by fluids and chemicals, pose significant challenges in thermal management. As a promising alternative, polymer-based microchannel heat exchangers offer advantages such as antifouling, corrosion resistance, lightweight, and cost savings.[5–7] Moreover, the low thermal conductivity often associated with polymeric heat exchangers can be overcome by the addition of fillers and efficient design combined with 3D printing fabrication.[5,8]

3D printing techniques like fused deposition modeling (FDM), stereolithography apparatus (SLA), and digital light processing (DLP) have been explored using a variety of engineering polymers. Various non-photosensitive resins including polypropylene (PP) and polyether ether ketone (PEEK) are applied for printing by the FDM method which generally gives low resolution.[9–12] In particular, the DLP method using photosensitive resin produces features with high resolution and complex parts in a short time by curing layer by layer.[3] Nonetheless, the practical application under various conditions is often hindered by the limitations of commercial organic resins, which typically exhibit low thermal stability, mechanical strength, and chemical resistance.[13–15]

Polymer-derived ceramics (PDCs) have been employed in the 3D printing approach to create 3D ceramic objects from preceramic polymers such as polycarbosilanes and subsequent conversion to the non-oxide SiC ceramic phase by high temperature pyrolysis over 1000 °C under an inert atmosphere.[16–18] Despite the robust properties of 3D-printed PDCs, the structures suffer from severe shrinkage during the pyrolysis process, which can deform or crack due to the large weight loss of gaseous by-products.[19] Notably, the cross-

Center for Intelligent Microprocess of Pharmaceutical Synthesis, Department of Chemical Engineering, Pohang University of Science and Technology (POSTECH), Pohang 37673, Korea. E-mail: dpkim@postech.ac.kr

† Electronic supplementary information (ESI) available. See DOI: https://doi.org/10.1039/d3re00694h

‡ These authors contributed equally to this work.

linked preceramic polymers offer higher thermal stability and chemical resistance than their organic counterparts.[20] At this point, the optimal choice of hybrid characteristics between polymers and ceramics would be interesting with some advantages over PDCs such as little shrinkage, higher versatility, and better optical properties, depending on the specific and desired performance of 3D-printed systems. Moreover, it requires to formulate the organic–inorganic hybrid resin with high photocuring kinetics by adding an acrylate monomer.[21,22] In addition, the organic–inorganic hybrid resin for DLP type 3D printing must be optimized in the cocktails of various additives as well as printing parameters.[23–26]

Herein, an organic–inorganic hybrid resin optimized for DLP type 3D printing is presented to fabricate MHEs with higher robustness over polymer heat exchangers. As illustrated in Scheme 1, the resin comprises a base blend of allylhydridopolycarbosilane (AHPCS) and 1,6-hexanediol diacrylate (HDDA) monomers, combined with a TPO photoinitiator, Sudan Orange G (SOG) resolution enhancer, and fumed silica anti-sticking agent. The SOG not only facilitates high-resolution printing through regulated light penetration, but also enables fabrication of hollow microchannel structures. Furthermore, the fumed silica promotes release from the resin vat for improved printability of micro-scale and high aspect ratio structures, while enhancing the mechanical stability of each cured layer. The 3D-printed organic–inorganic hybrid polymer showed improved thermo-physical properties such as modulus, hardness, thermal conductivity, and the coefficient of thermal expansion compared to commercial 3D-printed PMMA through a thermally post-curing process. Eventually, the 3D-printed and post-cured tube-in-tube type microchannel heat exchangers (3P-TMHEs) were designed and fabricated *via* a DLP type 3D printer using hybrid resin. The 3P-TMHE was demonstrated using DMSO at 70 °C to evaluate the heat exchange efficiency to show thermal and chemical stability.

Experimental

Materials

The inorganic polymer AHPCS (SMP-10) was acquired from Starfire Systems (USA). The difunctional acrylate monomer 1,6-hexanediol diacrylate (HDDA), the photoinitiator diphenyl(2,4,6-trimethylbenzoyl)phosphine oxide (TPO), and the resolution enhancer Sudan Orange G (SOG) were purchased from Sigma Aldrich. The fumed silica filler (AEROSIL OX 50, 40 nm) was obtained from Evonik. The DLP type 3D printer (PICO 2 HD) and the commercial poly(methyl methacrylate) resin (PMMA, PlasCLEAR v2) were purchased from Asiga (Australia). The PEEK nut (XP-235), luer adapter (P-628), and PTFE tubing (1/16″ O.D., 0.039″ I.D.) were procured from IDEX Health & Science. The syringe and syringe pump were purchased from HENKE-JECT and Harvard Apparatus (USA), respectively.

Formulation of the organic–inorganic hybrid resin

To achieve optimal 3D-printed structures, numerous variables such as 3D printing parameters (*e.g.*, light intensity, exposure time of layer) and the ratio of resin formulation (*i.e.*, oligomer, monomer, photoinitiator, and additives) were carefully considered. To simplify these variables, the organic–inorganic hybrid resin was formulated based on a light intensity of 3 mW cm^{-2} and an exposure time of 6 s per layer. The difunctional acrylate monomer HDDA, which acts as a cross-linker in the resin system and enhances the curing kinetics during photopolymerization with AHPCS, was used to dissolve the additives, such as TPO and SOG, and to lower the viscosity of the resin. The base resin was prepared by mixing 52.3 wt% of AHPCS and 47.7 wt% of HDDA, where the content of inorganic polymer in a previous study by Nabat Al-Ajrash *et al.* was slightly improved.[22] To prepare the resin for use in a DLP type 3D printer, TPO (0–0.6 wt% of base resin) and SOG (0–0.05 wt% of base resin) were added to the HDDA and stirred for 1 h. Fumed silica (0–25 wt% of base resin, 40 nm) was added to the HDDA and sonicated for 30 min to achieve a stable dispersion. The organic–inorganic hybrid resin which blended AHPCS and HDDA with cocktails of additives was sonicated for 10 min and stirred for 3 h before use in the DLP type 3D printer. After finding the optimal amount of each additive, four compositions of the organic–inorganic hybrid resin were formulated to investigate the role of each additive (Table 1).

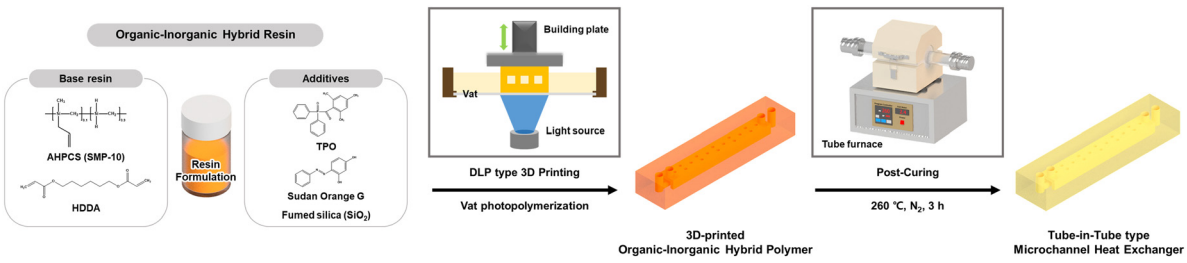

Scheme 1 Scheme of the tube-in-tube type microchannel heat exchanger *via* a DLP type 3D printer. The organic–inorganic hybrid resin is formulated with AHPCS, HDDA, and additives (TPO, SOG, fumed silica) to employ a commercial DLP type 3D printer.

Table 1 Formulation of the organic–inorganic hybrid resin with different ratios of additives

	Base resin (wt%)		Additives (wt% of base resin)		
Entry	AHPCS	HDDA	TPO	SOG	Fumed silica
Hybrid 1	52.3	47.7	0.5	—	—
Hybrid 2	52.3	47.7	0.5	0.02	—
Hybrid 3	52.3	47.7	0.5	—	15
Hybrid 4	52.3	47.7	0.5	0.02	15

Fabrication and post-curing of the 3D-printed organic–inorganic hybrid polymer

3D modeling of the heat exchanger proceeded using Autodesk Inventor Professional software (version 2019) and it was sliced to a thickness of 50 μm and additively manufactured into layers of the same thickness by irradiating the pattern with UV light. The DLP type 3D printer was operated at a wavelength of 385 nm and a pixel size of 27 μm. To take advantage of the fast production speed of 3D printing, all structures were cured with an exposure time of 6 s per layer. The hybrid 1–4 resin samples and commercial PMMA resin were cured with a light intensity of 3 mW cm^{-2} and 10 mW cm^{-2}, respectively. The 3D-printed structures were rinsed with isopropyl alcohol (IPA) to remove any residual resin. The 3D-printed structure fabricated using hybrid 4 was thermally post-cured at 260 °C at a heating rate of 1 °C min^{-1} in a tube furnace, maintained for 3 h, and then slowly cooled to room temperature at a cooling rate of 1 °C min^{-1}.

Heat resistance and chemical resistance of the 3D-printed and post-cured organic–inorganic hybrid polymer

To investigate their heat resistance, the weight loss and expansion in length of cube (3 × 3 × 3 mm^3) and cuboid (3 × 3 × 10 mm^3) samples of the 3D-printed hybrid 4, post-cured hybrid 4, and 3D-printed PMMA were observed as the temperature increased from 25 to 800 °C and 25 to 300 °C. In order to test their chemical resistance, the 3D-printed hybrid 4, post-cured hybrid 4, and 3D-printed PMMA (3 × 3 × 3 mm^3) were immersed in various organic solvents (acetone, acetonitrile, ethanol, *N*,*N*-dimethylformamide, dimethyl sulfoxide) for 24 h at room temperature, as well as dimethyl sulfoxide (DMSO) at 150 °C for 24 h. The swelling ratio was calculated as follows:

$$\text{Swelling ratio (\%)} = \frac{W_2 - W_1}{W_1} \times 100$$

where W_1 and W_2 are the weights before and after immersion, respectively.

Design and evaluation of 3P-TMHEs

The 3P-TMHE (11 × 7 × 46 mm^3) which has a tube-in-tube structure consists of an inner channel (1 × 1 × 40 mm^3) and an annular outer channel (5 × 3 × 36 mm^3) surrounding the inner channel. Inside of the outer channel, pillar structures (diameter 1 mm, height 1 mm) were designed as supports of the channel ceiling. The performance of 3P-TMHEs on resin and in the fluid flow direction was evaluated through a series of computational fluid dynamics (CFD) simulations in COMSOL Multiphysics 6.0. Additionally, to assess the actual performance of the 3P-TMHE, a syringe pump was utilized to connect a syringe to the 3P-TMHE *via* PTFE tubing. The outlet temperature was measured for flow rates ranging from 500 μl min^{-1} to 1500 μl min^{-1} by flowing DMSO at 70 °C as the hot fluid and water at 20 °C as the cold fluid. The logarithmic mean temperature difference (LMDT) was calculated using the following equations:

$$\text{LMDT (Parallel flow)} = \frac{(T_1 - t_1) - (T_2 - t_2)}{\ln \frac{(T_1 - t_1)}{(T_2 - t_2)}}$$

$$\text{LMDT (Counter flow)} = \frac{(T_1 - t_2) - (T_2 - t_1)}{\ln \frac{(T_1 - t_2)}{(T_2 - t_1)}}$$

where T_1 and T_2 are the inlet and outlet temperatures of hot fluid and t_1 and t_2 are the inlet and outlet temperatures of cold fluid, respectively.

Characterization

To optimize the formulation of the organic–inorganic hybrid resin, various experiments were conducted. First, to match suitable additives for the light source of the DLP type 3D printer, the absorbance of photoinitiator TPO and resolution enhancer SOG was measured using a spectrophotometer (NanoDrop 2000c, Thermo Fisher Scientific), respectively. The curing depth and edge shape of the honeycomb pattern were investigated by taking images with a microscope (Eclipse Ti–U, Nikon Instruments) at fixed light intensity and exposure time of each layer to determine the optimal concentration of TPO and SOG. The viscosity of the organic–inorganic hybrid resin with fumed silica was examined using a rheometer (MCR 102, Anton Paar) to determine the optimal concentration of fumed silica for application with a DLP type 3D printer. The dispersion stability of fumed silica was verified by observing cross-sectional images of the cured film using a scanning electron microscope (SEM; S-4800, Hitachi). For the formulation of hybrids 1–4, cylinders with a diameter and height of 800 μm were 3D-printed and observed using SEM to confirm the effect of additives on 3D-printed structures. The thermal conductivity of the organic–inorganic hybrid polymer was calculated using the flash method, which is a non-contact measurement method, by multiplying the thermal diffusivity, specific heat, and bulk density. The thermal diffusivity was measured using a light flash apparatus (LFA; LFA 467 HyperFlash, Netzsch), while the specific heat was obtained using a differential scanning calorimeter (DSC; DSC 204 F1 Phoenix, Netzsch). The bulk

density was measured using Archimedes' principle. The weight loss was measured using a thermogravimetric analyzer (TGA; Q600 SDT, TA Instrument). The coefficient of thermal expansion, elastic modulus, and hardness were determined using a thermomechanical analyzer (TMA; TMA 402 F3 Hyperion, Netzsch) and nanoindentation (TI 750L, Hysitron).

Results and discussion

Additive effect on the organic–inorganic hybrid resin for a 3D printer

The DLP type 3D printer operates on a bottom-up approach and requires low-viscosity, rapid consolidation by vat photopolymerization. To improve the photocuring kinetics, the photocurable organic–inorganic hybrid resin was formulated by mixing AHPCS with vinyl functional groups and HDDA with acrylate functional groups in a weight ratio of 52.3 : 47.7, referred to as the base resin. However, the ratio of AHPCS cannot exceed 52.3% due to the lower photocuring kinetics of vinyl functional groups, which makes it difficult to apply to a DLP type 3D printer. The photoinitiator, which absorbs light energy from a specific wavelength of the light source to initiate photopolymerization, is an additive that affects the degree of curing. In addition, a resolution enhancer, SOG, which is a UV absorber, was added to limit the penetration depth of light and absorb scattered light to achieve high-resolution microstructures. TPO was selected as the photoinitiator, and SOG was selected as the resolution enhancer due to their high absorption spectra at the 385 nm wavelength of the 3D printer light source, as shown in Fig. S1.† When TPO absorbs UV light, the P–C bond is cleaved and it undergoes a transition from the ground state to the excited state, resulting in two free radicals that initiate photopolymerization.[27] To investigate the effect of TPO on the curing behaviour, the curing depth was measured at various concentrations of TPO with the base resin, at a light intensity of 3 mW cm^{-2} and an exposure time of 6 s per layer. At TPO concentrations of 0, 0.05 and 0.1 wt%, the base resin did not cure. However as shown in Fig. 1a, as the concentration of TPO increased from 0.15 to 0.6 wt%, the curing depth increased from 4.2 μm to 90.6 μm. Although the target thickness of the layer cured by slicing in the 3D printer is 50 μm, the optimal concentration of TPO was found to be 0.5 wt% with a curing depth of 77 μm, due to a decrease in curing depth with increasing concentration of SOG. The SOG was added to the optimized TPO-added base resin. To assess the effect of SOG on the resolution enhancement, the curing depth as in Fig. 1b and resolution of the honeycomb pattern as in Fig. 1c and e were measured at a light intensity of 3 mW cm^{-2} and an exposure time of 6 s per layer. As the concentration of SOG increased from 0 to 0.05 wt%, the curing depth decreased from 77 to 21 μm. At a concentration of 0.02 wt% of SOG, a curing depth of 51 μm was achieved, which was similar to the target curing depth of

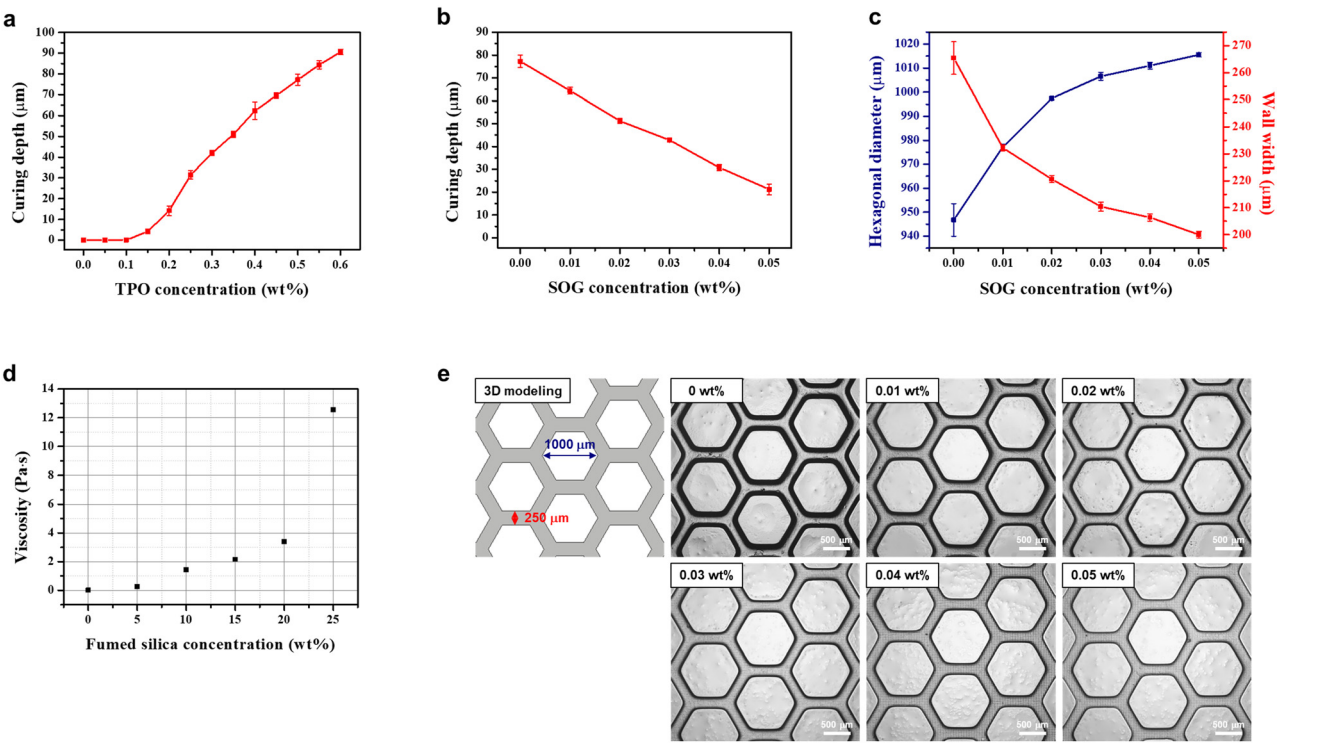

Fig. 1 Effect of additives on 3D printability. Curing behaviour according to (a) TPO concentration and (b) SOG concentration. (c) Hexagonal pattern shape according to SOG concentration. (d) Viscosity of the resin containing 0.5 wt% of TPO and 0.02 wt% of SOG for different concentrations of fumed silica at a 5 s^{-1} shear rate. (e) 3D modeling image and microscopy images of the 3D-printed hexagonal pattern according to SOG concentration.

50 μm. Additionally, the hexagonal diameter and wall thickness at 0.02 wt% of SOG were 997.4 μm and 220.6 μm, respectively, which were the most similar to the 1000 μm and 250 μm of the 3D modeling. When SOG was added, the edges of the honeycomb pattern became sharp, similar to the 3D modeling, resulting in significant enhancement of printing resolution.

The incorporation of fumed silica as an inorganic filler in the organic–inorganic hybrid resin not only acts as an anti-sticking agent, facilitating easy release of the 3D-printed layer from the vat, but also improves printability by enhancing the mechanical properties of the layer. For successful DLP type 3D printing, the resin's rheological behaviour should exhibit shear thinning of a non-Newtonian fluid and have a viscosity of less than 3 Pa s to enable self-levelling and recoating.[28–31] To investigate the rheological behaviour and the dispersion stability of fumed silica, the resin and cured films with a thickness of 1 mm were prepared by filling with 0 to 25 wt% of fumed silica to the optimal TPO and SOG-added organic–inorganic hybrid resin. At the 3D printer's casting shear rate of 5 s^{-1}, the viscosity increased with increasing fumed silica concentration, as shown in Fig. 1d. The viscosity at 15 wt% of fumed silica was 2.16 Pa s, exhibiting appropriate rheological behaviour, while the viscosity at 20 to 25 wt% of fumed silica exceeded 3 Pa s. Additionally, with 25 wt% of fumed silica, a sharp increase in viscosity at the shear rate of 5 s^{-1} was observed, and the cross-sectional SEM images of the cured films revealed aggregation of fumed silica (Fig. S2†).

Through comprehensive investigations of various additives, four distinct formulations (hybrids 1–4) were developed, with the detailed compositions summarized in Table 1. To assess the 3D printability of each formulation, a micro-structured cylinder (diameter of 800 μm and height of 800 μm) was printed as shown in Fig. 2a. The use of hybrid 1 and hybrid 2 without fumed silica resulted in failed 3D printing at a light intensity of 3 mW cm^{-2}. Despite over-curing the layers with a light intensity of 15 mW cm^{-2}, to address the inherent problem of the bottom-up DLP type 3D printer (*i.e.*, vat photopolymerization) where the cured layer adheres to the vat due to weak mechanical properties, the circular layer with an 800 μm diameter was adhered to the vat and was torn. However, the use of hybrid 3 and hybrid 4 with fumed silica facilitated 3D printing at a light intensity of 3 mW cm^{-2}, owing to the improved mechanical strength of the layer and anti-sticking effect. Notably, hybrid 4 containing SOG and fumed silica yielded a micro-structured cylinder with improved resolution, which rendered a close resemblance to that of 3D modeling. Nanoindentation was performed on the surface of the 3D-printed layers of hybrid 2 (without fumed silica), hybrid 4 (with fumed silica), and PMMA (commercial resin) to determine the modulus and hardness in Fig. 2b and c. The hybrid 2 layer exhibited 0.017 GPa modulus and 0.002 GPa hardness, which were significantly lower than those of the PMMA layer. In contrast, the hybrid 4 layer displayed 0.055 GPa modulus and 0.005 GPa hardness, which were improved from the hybrid 2.

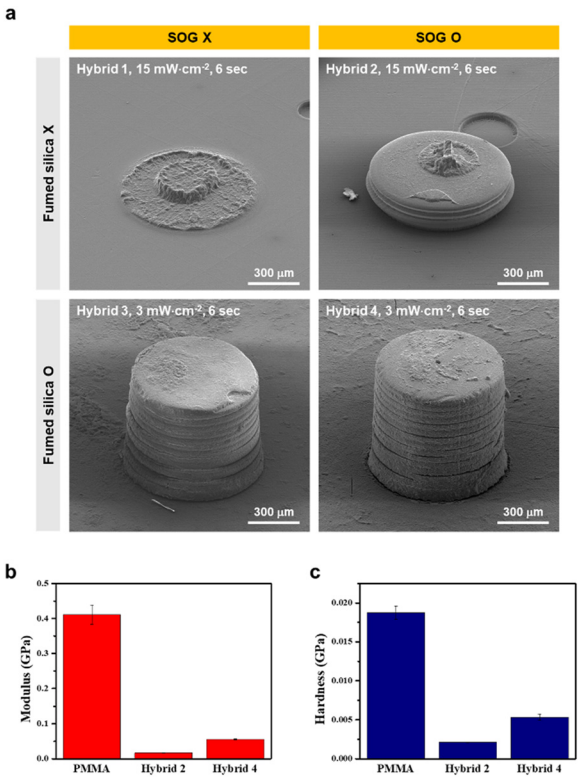

Fig. 2 (a) Effect of SOG (0.02 wt%) as a resolution enhancer and fumed silica (15 wt%) as an anti-sticking agent, as SEM images of 3D-printed cylinders. (b) Modulus and (c) hardness of 3D-printed PMMA, hybrid 2, and hybrid 4.

Hybrid 4 showed high printability through improved modulus and hardness.

Volume shrinkage during photopolymerization which uses acrylates can cause dimensional errors when 3D printing microchannel structures.[32,33] To characterize this, square and circular microchannels (100–2000 μm) were printed and measured using hybrid 4 as shown in Fig. S3.† Channels were 118–176 μm smaller than 3D modeling due to shrinkage. Furthermore, square channels over 1200 μm collapsed due to ceiling rupture, increasing the vertical error up to 139 μm. Thus, the minimum printable size was 500 μm (square) and 600 μm (circular) while the maximum printable square channel size without supports was 1200 μm.

Post-curing effect of the 3D-printed organic–inorganic hybrid polymer

It was reported that the mechanical properties of photocured inorganic polymers were generally improved by additional thermal curing.[20,34] In the case of the organic–inorganic hybrid resin, AHPCS was photopolymerized with HDDA through allyl-acrylate co-polymerization.[21] Therefore, unreacted Si–H and allyl functional groups would still remain to be further thermally cross-linked by post-curing.[35] To investigate the post-curing temperature of 3D-printed structures from hybrid 4, differential scanning calorimetry

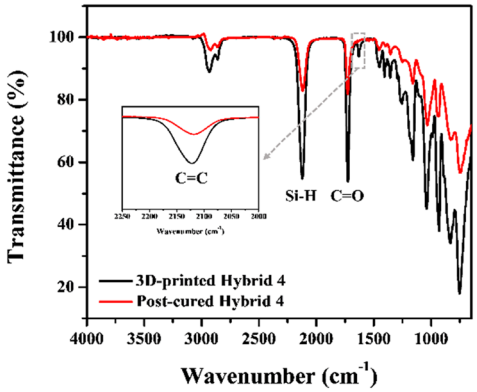

Fig. 3 ATR-FTIR spectra of 3D-printed and post-cured hybrid 4 samples.

(DSC) analysis was conducted. The polymerization peak was observed at 240–260 °C in the thermal scanning mode, while the peak disappeared with the post-cured sample at 260 °C for 3 h (Fig. S4†). Moreover, when the post-cured hybrid 4 sample was analysed by ATR-FTIR in Fig. 3, the Si–H (2120 cm^{-1}) and C═C (1631 cm^{-1}) peaks considerably decreased, presumably due to hydrosilylation and dehydrogenative coupling reactions upon post-curing. After post-curing, the structures changed from orange colour to pale yellowish due to thermal decomposition of SOG starting at 180 °C[36] and were observed to undergo isotropic shrinkage of 2% (Fig. S4†).

At this stage, the thermo-physical properties of hybrid 4 were comprehensively investigated to evaluate the effect of post-curing at 260 °C for 3 h. As shown in Fig. 4a and b, the modulus and hardness of 3D-printed hybrid 4 were initially lower than those of 3D-printed PMMA. However, post-cured hybrid 4 was found to have 3.5 times higher modulus and 7.8 times stronger hardness compared to 3D-printed PMMA. These results confirm the significant enhancement of mechanical properties achieved by the highly cross-linked polymeric network of the post-cured hybrid 4.

Furthermore, thermal conductivities of 3D-printed PMMA, 3D-printed hybrid 4, and post-cured hybrid 4 were obtained by calculating the product of thermal diffusivity, specific heat, and bulk density, and the detailed results are noted in Table S1.† Both 3D-printed PMMA and 3D-printed hybrid 4 exhibited similar thermal conductivity values of 0.2 W m^{-1} K^{-1}, which is typical for general polymers. However, the thermal conductivity of the post-cured hybrid 4 was obviously improved by 15% to 0.23 W m^{-1} K^{-1} as shown in Fig. 4c.

The coefficient of thermal expansion and heat resistance were also measured to demonstrate the enhanced properties for post-curing of 3D-printed structures. In Fig. 4d, the slope of the dimension change is the average coefficient of thermal expansion. The results showed that 3D-printed PMMA had a higher coefficient of thermal expansion of 160.87 ppm K^{-1} compared to post-cured hybrid 4, which had a coefficient of 132.80 ppm K^{-1}. Additionally, the length of 3D-printed hybrid 4 rapidly decreased at around 195 °C, and then increased again at about 235 °C, indicating that volume shrinkage due to post-curing polymerization occurred between 195 and 235 °C. As shown in Fig. 4e, thermogravimetric analysis (TGA) was performed in a temperature range of 25 to 800 °C. It was observed that both 3D-printed PMMA and 3D-printed hybrid 4 underwent gradual thermal decomposition starting from 50 °C. At 330 °C, the weight loss of 3D-printed PMMA and 3D-printed hybrid 4 was 6% and 2%, respectively. In contrast, thermal decomposition of the post-cured hybrid 4 started at a significantly higher temperature of 330 °C. These results confirm that post-cured hybrid 4 has superior thermal

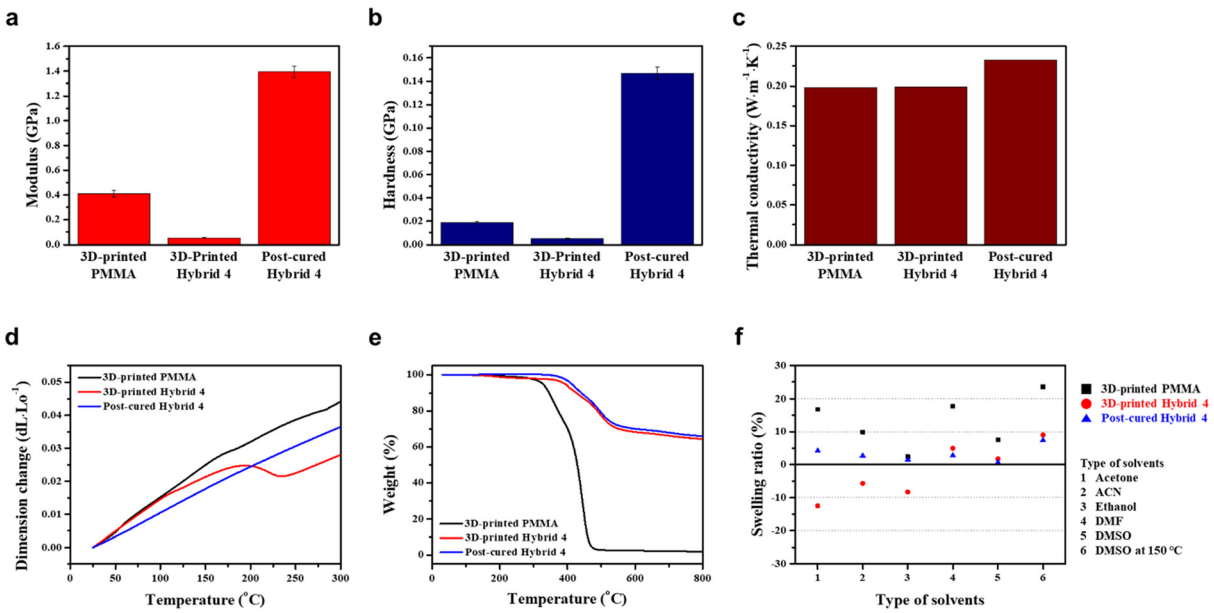

Fig. 4 Comparative thermo-physical properties of 3D-printed PMMA, 3D-printed hybrid 4, and post-cured hybrid 4. (a) Modulus, (b) hardness, (c) thermal conductivity, (d) coefficient of thermal expansion, (e) weight loss, and (f) swelling ratio in various organic solvents.

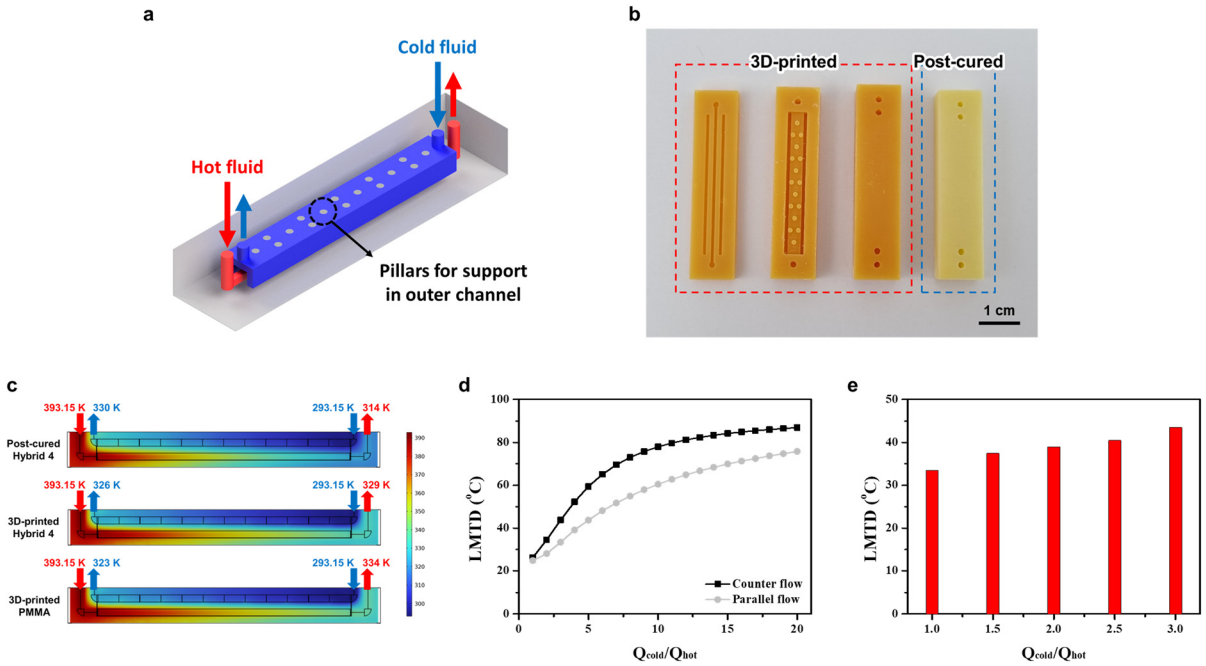

Fig. 5 (a) 3D modeling of the TMHE. (b) 3D-printed TMHE without a ceiling, 3D-printed TMHE with a ceiling, and post-cured TMHE. (c) Heat exchange comparison of 3D-printed PMMA, 3D-printed hybrid 4, and post-cured hybrid 4 using CFD simulation. (d) CFD simulated LMDT of counter flow and parallel flow according to $Q_{cold}{\cdot}Q_{hot}^{-1}$. (e) Experimented LMTD of counter flow according to $Q_{cold}{\cdot}Q_{hot}^{-1}$.

dimensional stability and thermal resistance compared to PMMA printed with commercial resin.

The chemical stability of the 3D-printed PMMA, 3D-printed hybrid 4, and the post-cured hybrid 4 was comparatively assessed by immersing them in various organic solvents (acetone, ACN, ethanol, DMF, and DMSO) at 25 °C for 24 h, as well as DMSO at 150 °C for 24 h (Fig. S5†). The swelling ratio was measured by weighing the samples before and after immersion. The 3D-printed PMMA had a swelling ratio range of 7.6–17.7% in those organic solvents at 25 °C, which was less in ethanol but showed significant swelling behaviour in acetone and DMF. The 3D-printed hybrid 4 was broken in all organic solvents except DMSO at 25 °C, which exhibited inferior chemical resistance to the 3D-printed PMMA. Notably, the decreased weight was attributed to partial dissolution of uncured resin in organic solvents. The post-cured hybrid 4, on the other hand, exhibited a swelling ratio of less than 5% in all organic solvents at 25 °C. Further, when immersed in DMSO at 150 °C, the post-cured hybrid 4 maintained an intact shape with a swelling ratio of 7.4%, which showed superior chemical resistance to the 3D-printed PMMA with a swelling ratio of 23.6% and the cracked 3D-printed hybrid 4 with a swelling ratio of 9% (Fig. 4f). These results indicate that the post-cured process of the hybrid 4 polymer renders potential for resistant heat exchanger applications.

Fabrication and evaluation of 3P-TMHEs

In the present investigation, a novel design of 3P-TMHEs was conceptualized and developed using a formulated resin, hybrid 4. To realize the tube-in-tube channel, the structural robustness of the outer channel was ensured by the strategic incorporation of pillar structures as supports, a necessity that was underscored by the 3D printability test of square channel microscopy images, as depicted in Fig. S3.† The comprehensive design of the heat exchanger, which was tailored for DLP type 3D printing, is graphically represented in Fig. 5a. The design features an inner microchannel, which serves as the conduit for the hot fluid, and an outer, more expansive channel that surrounds the hot flow and facilitates the flow of the cold fluid as an actual heat exchanger shown in Fig. 5b, Notably, the optimal channel width (1 mm) of the cold fluid was numerically determined as shown in Fig. S6.† To gauge the performance of the heat exchanger, the CFD simulation incorporated the governing equations pertinent to liquid and solid heat transfer either for convection or conduction heat transfer, in addition to those governing laminar flow such as Navier–Stokes coupled with continuity equations. The performance of the 3P-TMHE is presented in Fig. 5d with the ratio of the cold fluid flow rate to the hot fluid flow rate serving as the *x*-axis and the LMTD constituting the *y*-axis. The hot fluid flow rate was held constant at 1 ml min^{-1}, while the cold fluid flow rate was progressively increased. Also, for accurate experimental evaluation, short tubing distances as well as proper insulation were considered, although the CFD simulation indicated little heat loss between the hot sand bath and the inlet of the heat exchanger (Fig. S7†). The fluids employed in the CFD simulation were DMSO for the hot fluid at 393.15 K and water for the cold fluid at 293.15 K. In particular, the counter flow exhibited superior performance

in comparison with the parallel flow. Based on this result, three types of TMHEs (3D-printed PMMA, 3D-printed hybrid 4, and post-cured hybrid 4) were computed under counter flow and the highest performance flow rate conditions ($Q_{cold}{\cdot}Q_{hot}^{-1}$ value is 20) using the thermal conductivities in Table S1.† As illustrated in Fig. 5c, the post-cured hybrid 4 outperformed the others, as evidenced by the lower outlet temperature of the hot fluid (314 K) compared to the 3D-printed PMMA (334 K) and 3D-printed hybrid 4 (329 K). As presented in Fig. S8,† the 3P-TMHE fabricated from hybrid 4 was experimented at a fixed inlet flow rate, 500 μl min^{-1}, of hot fluid (DMSO) at 70 °C while the inlet flow rate of cold fluid (water) was increased at 20 °C. Similar to the CFD simulation results, as the $Q_{cold}{\cdot}Q_{hot}^{-1}$ value increased from 1 to 3, the LMTD also increased from 33.4 °C to 43.5 °C, as shown in Fig. 5e.

Conclusions

In summary, the parameter study of 3D printing an organic–inorganic hybrid resin was performed by formulating with cocktails of additives for 3P-TMHE. Through hybrid 4 where 0.5 wt% of TPO, 0.02 wt% of SOG, and 15 wt% of fumed silica were added, high-resolution microscale and hollow structures were rendered. The thermo-physical properties of 3D-printed hybrid 4 were highly improved upon thermal post-curing at 260 °C for 3 h, which were superior to those of 3D-printed PMMA. And the 3P-TMHE was designed by screening the size of the printable channel with less dimensional errors which caused volume shrinkage during photopolymerization. Upon 3D printing, the pillar structures in the 3P-TMHE were required to support the channel ceiling with no collapse. And the thermally and chemically resistant 3P-TMHE in DMSO at 70 °C showed a higher LMTD at the increasing flow rate ratio, $Q_{cold}{\cdot}Q_{hot}^{-1}$, under counter flow conditions as revealed by CFD simulation. These results indicated that the organic–inorganic hybrid resin has the potential to be used not only in 3D-printed heat exchangers but also in chemical engineering fields.

Conflicts of interest

The authors declare that they have no known competing financial interests or personal relationships that could have appeared to influence the work reported in this paper.

Acknowledgements

This work was financially supported by the Institute of Civil-Military Technology Cooperation funded by the Defense Acquisition Program Administration and Ministry of Trade, Industry and Energy of Korean government (No. 21-CM-CE-03) and the National Research Foundation (NRF) of Korea grant funded by the Korean government (MSIP) (NRF-2017R1A3B1023598).

Notes and references

1 H. Lim, U. Han and H. Lee, *Appl. Therm. Eng.*, 2020, **165**, 114609.
2 J. Bohacek, M. Raudensky and E. Karimi-Sibaki, *Appl. Therm. Eng.*, 2019, **159**, 113940.
3 L. Kelava, I. Ivić, E. Pakai, K. Fekete, P. Maroti, R. Told, Z. Ujfalusi and A. Garami, *Polymers*, 2022, **14**, 1–16.
4 M. V. Rane and Y. S. Padiya, *Energy Sustainable Dev.*, 2011, **15**, 184–191.
5 B. Ahmadi and S. Bigham, *Appl. Therm. Eng.*, 2022, **204**, 117993.
6 D. C. Deisenroth, R. Moradi, A. H. Shooshtari, F. Singer, A. Bar-Cohen and M. Ohadi, *Heat Transfer Eng.*, 2018, **39**(19), 1652–1668.
7 A. R. J. Hussain, A. A. Alahyari, S. A. Eastman, C. Thibaud-Erkey, S. Johnston and M. J. Sobkowicz, *Appl. Therm. Eng.*, 2017, **113**, 1118–1127.
8 X. Chen, Y. Su, D. Reay and S. Riffat, *Renewable Sustainable Energy Rev.*, 2016, **60**, 1367–1386.
9 E. G. Gordeev, E. S. Degtyareva and V. P. Ananikov, *Russ. Chem. Bull.*, 2016, **65**, 1637–1643.
10 M. J. Harding, S. Brady, H. O'Connor, R. Lopez-Rodriguez, M. D. Edwards, S. Tracy, D. Dowling, G. Gibson, K. P. Girard and S. Ferguson, *React. Chem. Eng.*, 2020, **5**, 728–735.
11 M. R. Penny and S. T. Hilton, *React. Chem. Eng.*, 2020, **5**, 853–858.
12 R. Thavarajah, M. R. Penny, R. Torii and S. T. Hilton, *J. Org. Chem.*, 2023, **88**, 16845–16853.
13 F. Kotz, P. Risch, D. Helmer and B. E. Rapp, *Micromachines*, 2018, **9**(3), 115.
14 A. Urrios, C. Parra-Cabrera, N. Bhattacharjee, A. M. Gonzalez-Suarez, L. G. Rigat-Brugarolas, U. Nallapatti, J. Samitier, C. A. Deforest, F. Posas, J. L. Garcia-Cordero and A. Folch, *Lab Chip*, 2016, **16**, 2287–2294.
15 G. N. Ahn, M. J. Kim, S. J. Yim, B. M. Sharma and D. P. Kim, *ACS Sustainable Chem. Eng.*, 2022, **10**, 3951–3959.
16 K. W. Gyak, N. K. Vishwakarma, Y. H. Hwang, J. Kim, H. S. Yun and D. P. Kim, *React. Chem. Eng.*, 2019, **4**, 1393–1399.
17 Z. C. Eckel, C. Zhou, J. H. Martin, A. J. Jacobsen, W. B. Carter and T. A. Schaedler, *Science*, 2016, **351**(6268), 58–62.
18 J. M. Hundley, Z. C. Eckel, E. Schueller, K. Cante, S. M. Biesboer, B. D. Yahata and T. A. Schaedler, *Addit. Manuf.*, 2017, **18**, 95–102.
19 R. He, N. Zhou and K. Zhang, *et al.*, *J. Adv. Ceram.*, 2021, **10**, 637–674.
20 W. Ren, J. Perumal, J. Wang, H. Wang, S. Sharma and D. P. Kim, *Lab Chip*, 2014, **14**, 779–786.
21 Y. de Hazan and D. Penner, *J. Eur. Ceram. Soc.*, 2017, **37**, 5205–5212.
22 S. M. N. Al-Ajrash, C. Browning, R. Eckerle and L. Cao, *Mater. Adv.*, 2021, **2**, 1083–1089.
23 C. I. Rogers, K. Qaderi, A. T. Woolley and G. P. Nordin, *Biomicrofluidics*, 2015, **9**(1), 016501.
24 J. Markarian, *Plast. Addit. Compd.*, 2007, **9**, 32–35.

25 T. Ribeiro, C. Baleizão and J. P. S. Farinha, *Materials*, 2014, **7**, 3881–3900.
26 T. D. Martins, T. Ribeiro and J. P. S. Farinha, *Polymers*, 2021, **13**, 1003.
27 T. Corrales, F. Catalina, C. Peinado and N. S. Allen, *J. Photochem. Photobiol., A*, 2003, **159**, 103–114.
28 C. Hinczewski, S. Corbel and T. Chartier, *J. Eur. Ceram. Soc.*, 1998, **18**, 583–590.
29 J. H. Jang, S. Wang, S. M. Pilgrim and W. A. Schulze, *J. Am. Ceram. Soc.*, 2000, **83**, 1804–1806.
30 X. Wang, *Thiol-Ene Click Chemistry Assisted Additive Manufacturing and Freeze Casting of Polymer-Derived Ceramics*, 2017, vol. 3.
31 Z. Li, Z. Chen, J. Liu, Y. Fu, C. Liu, P. Wang, M. Jiang and C. Lao, *Virtual Phys. Prototyp.*, 2020, **15**, 163–177.
32 J. W. Park, G. S. Shim, J. H. Back, H. J. Kim, S. Shin and T. S. Hwang, *Polym. Test.*, 2016, **56**, 344–353.
33 S. Schoerpf, Y. Catel, N. Moszner, C. Gorsche and R. Liska, *Polym. Chem.*, 2019, **10**, 1357–1366.
34 M. J. Assael, S. Botsios, K. Gialou and I. N. Metaxa, *Int. J. Thermophys.*, 2005, **26**, 1595–1605.
35 K. W. Gyak, S. Jeon, L. Ha, S. Kim, J. Young Kim, K. S. Lee, H. Choi and D. P. Kim, *Adv. Healthcare Mater.*, 2019, **8**, 1–7.
36 T. L. Nguyen and M. A. Saleh, *Results Chem.*, 2020, **2**, 100085.